# Traveling wave analysis of non-thermal far-field blooming in high-power broad-area lasers

Anissa Zeghuzi[1], Mindaugas Radziunas[2], Hans-Jürgen Wünsche[1,2],

Jan-Philipp Koester[1], Hans Wenzel[1], Uwe Bandelow[2], Andrea Knigge[1]

submitted: October 17, 2019

[1]  Ferdinand-Braun-Institut
   Leibniz Institut für Höchstfrequenztechnik
   Gustav-Kirchhoff-Straße 4
   12489 Berlin
   Germany
   E-Mail: anissa.zeghuzi@fbh-berlin.de
         hans-juergen.wuensche@fbh-berlin.de
         jan-philipp.koester@fbh-berlin.de
         hans.wenzel@fbh-berlin.de
         andrea.knigge@fbh-berlin.de

[2]  Weierstrass Institute
   Mohrenstr. 39
   10117 Berlin
   Germany
   E-Mail: mindaugas.radziunas@wias-berlin.de
         hans-juergen.wuensche@wias-berlin.de
         uwe.bandelow@wias-berlin.de

# Traveling wave analysis of non-thermal far-field blooming in high-power broad-area lasers

Anissa Zeghuzi, Mindaugas Radziunas, Hans-Jürgen Wünsche, Jan-Philipp Koester, Hans Wenzel, Uwe Bandelow, Andrea Knigge

**Abstract**

With rising current the lateral far-field angle of high-power broad-area lasers widens (far-field blooming) which can be partly attributed to non-thermal effects due to carrier induced refractive index and gain changes that become the dominant mechanism under pulsed operation. To analyze the non-thermal contribution to far-field blooming we use a traveling wave based model that properly describes the injection of the current into and the diffusion of the carriers within the active region. Although no pre-assumptions regarding the modal composition of the field is made and filamentation is automatically accounted for, the highly dynamic time-dependent optical field distribution can be very well represented by only few modes of the corresponding stationary waveguide equation obtained by a temporal average of the carrier density and field intensity. The reduction of current spreading and spatial holeburning by selecting proper design parameters can substantially improve the beam quality of the laser.

## 1   Introduction

High-power semiconductor lasers emitting in the visible and near-infrared wavelength ranges are used as pump sources for high-performance laser systems but can also be employed for other applications such as direct material processing. The highest power can be achieved with broad area (BA) lasers with a width of the p-contact stripe ranging from tens to hundreds of micrometers, see Fig. 1. Due to the large emission aperture, BA lasers suffer from a poor beam quality, in particular from a far-field divergence exceeding the diffraction limit already slightly above threshold. However, to fully replace solid-state lasers by the more power-efficient BA lasers not only a high output power but also a small lateral far-field angle is needed.

Under continuous wave operation, the broadening of the lateral far-field with rising output power can be mainly attributed to the thermal lensing-effect caused by self-heating (thermal far-field blooming [1, 2, 3]). But there are also non-negligible non-thermal contributions as a result of the interplay between current spreading [4], lateral carrier diffusion and accumulation [5] and spatial holeburning. Non-thermal far-field blooming becomes the dominant effect under pulsed operation with current pulses long compared to the turn-on time combined with a very small repetition rate to avoid device heating.

Since many years, the multi-peaked and not diffraction-limited lateral field profiles of BA lasers are often interpreted in terms of filamentation. As shown in Ref. [6], a spontaneous break-up of the optical field into small filaments can happen in media with a focusing Kerr-nonlinearity. In semiconductor lasers an indirect Kerr-type nonlinearity can be induced by the dependence of the refractive index on the carrier density which in turn depends on the field intensity via the rate of stimulated recombination [7]. Early results of simulations based on a Maxwell-Bloch type dynamic traveling-wave model with a sophisticated treatment of carrier kinetics supported this view [8]. However, this model and later ones

[9] do not describe the current flow in a real device and have not been used in the context of far-field blooming. This way it remains unclear whether the reported filaments are indeed of Kerr-type or have another origin.
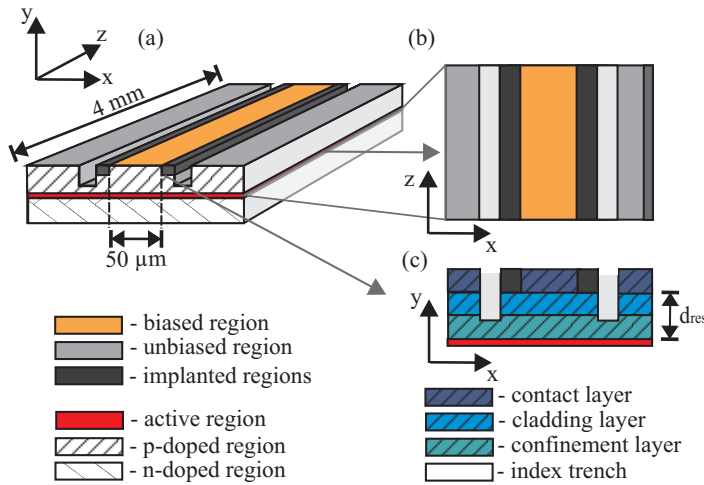


Figure 1: Schematic representation of the (a) simulated BA laser, (b) the longitudinal–lateral $(x, z)$ and (c) the lateral–vertical $(x, y)$ domain of simulations.

An alternative understanding of far-field blooming in BA lasers bases on co-lasing of multiple lateral waveguide modes [10]. Single mode emission becomes unstable just above threshold because, due to lateral spatial holeburning, any mode saturates the gain only in those parts of the active layer where the mode intensity is high. The gain in other parts rises with current, bringing more and more modes to threshold. The far-field widens because the far-field angle increases with mode number (e.g. Fig. 4(b)). Concerning non-thermal blooming, this picture has been supported by a stationary model based on the incoherent superposition of multiple modes [4]. However, the excitation of several lateral modes with different wavelengths leads to mode beating that drives oscillations of the occupation inversion via the stimulated emission. Thus, BA lasers exhibit an inherently non-stationary and highly non-linear behavior and the assumption of stationary multimode conditions is questionable [11]. Indeed, stationary laser models do not converge at high optical output powers [12, 13], so that far-field blooming effects cannot be studied far above threshold where state-of-the-art devices are operating.

In this paper we use an improved version of the software tool BALaser [14]. Based on a traveling-wave model, there are no ad-hoc assumptions of modes or stationarity and it includes the possibility of filamentation. A correct description of the current flow in the p-doped region which is crucial for non-thermal blooming is obtained by a solution of the Laplace equation for the quasi-Fermi potential of holes employing appropriate boundary conditions [15, 16]. Longitudinal inhomogeneity in the devices with highly asymmetric reflectivities is also taken into account, which implies a longitudinally-nonuniform distribution of the injected current [15], and has been shown to be crucial for thermal far-field blooming [3].

## 2   Device structure and numerical model

In what follows we briefly describe the studied device structure and the basic model equations.

The main parameters of the simulated device schematically drawn in Fig. 1 are as follows. The laser emitting at a central wavelength of $\lambda_0 = 970$ nm has rear and front facet power reflectivities of $R_0 = 0.95$ and $R_L = 0.01$, respectively. The active region consists of a $7$ nm thick single InGaAs quantum well and the p-doped region of contact (thickness $d = 130$ nm, conductivity $\sigma = 26680 \ (\Omega\text{m})^{-1}$),

cladding ($d = 445$ nm, $\sigma = 1660\,(\Omega\text{m})^{-1}$) and optical-confinement ($d = 770$ nm, $\sigma = 163\,(\Omega\text{m})^{-1}$) layers. The corresponding series resistivity of the structure is $r_\text{s} = \sum_{i=1}^{3} d_i/\sigma_i \approx 5 \cdot 10^{-9}\,\Omega\text{m}^2$. The cavity length is $L = 4$ mm and the width of the contact stripe on top of the p-doped region is $W = 50\,\mu$m. To provide lateral optical confinement $5\,\mu$m wide and $0.745\,\mu$m deep trenches filled with an insulator are located at a distance of $5\,\mu$m beside the stripe. Further details on the device structure can be found in Ref. [17]. Additional lateral current confinement can be obtained by implanting parts of the p-doped layers beside the contact stripe starting from the top layer. The residual layer thickness $d_\text{res}$ exemplary displayed in Fig. 1(c) gives the spacing between the active layer and the bottom of the implanted region with vanishing electrical conductivity.

As discussed earlier, models based on a stationary approximation of the optical field that either use an expansion into linear waveguide modes [4] or a beam propagation method [18] are not able to properly describe the inherently non-stationary behavior of BA lasers. Thus we use for the description of the optical field a time-dependent traveling-wave based model in the framework of the rotating-wave, slowly-varying-amplitude, and paraxial approximations. Here the optical field is given by the superposition of two counter propagating TE-polarized waves with the amplitudes $u^\pm(x, z, t)$ which are considered to be slowly varying with respect to the longitudinal position $z$ and time $t$. They obey,

$$\frac{1}{v_\text{g}}\partial_t u^\pm \pm \partial_z u^\pm = -\frac{i}{2\bar{n}k_0}\partial_x^2 u^\pm - ik_0\Delta n_\text{eff}u^\pm - \mathcal{D}u^\pm + f_\text{sp}^\pm \tag{1}$$

with reflecting boundary conditions at the facets. Here, $x$, $v_\text{g}$, $\bar{n}$, $k_0 = 2\pi/\lambda_0$ and $f_\text{sp}$ are the lateral position, group velocity, a real-valued reference index, a reference vacuum wave number and the spontaneous emission contribution the to optical field, respectively. The deviation

$$k_0\Delta n_\text{eff}(x, z, N) = k_0\Delta n_0(x, z) + k_0\Delta n_N(x, z, N) \tag{2}$$

$$+\frac{i}{2}\left[g(x, z, N, \|u\|^2) - \alpha(x, z, N)\right]$$

of the wave number from $k_0\bar{n}$ comprises built-in modifications of the effective index $\Delta n_0$ due to etched index trenches with $\Delta n_0 = -1.7 \cdot 10^{-3}$ for $(x, z) \in$ index trench and $\Delta n_0 = 0$ elsewhere, carrier density $N$ induced index contributions $\Delta n_N = -\sqrt{n'_N N}$ as well as gain $g = g'\ln(N/N_\text{tr})/(1 + \epsilon_\text{s}\|u\|^2)$ and losses $\alpha = \alpha_0 + f_N N$, where $n'_N = 4 \cdot 10^{-32}$ m$^3$, $g' = 2300$ m$^{-1}$, $N_\text{tr}$, $\epsilon_\text{s} = 6.8 \cdot 10^{-26}$ m$^3$, $\alpha_0 = 40$ m$^{-1}$, $f_N = 1.1 \cdot 10^{-23}$ m$^2$, and $\|u\|^2 = |u^+|^2 + |u^-|^2$ are the differential modal effective index, the differential modal gain, the transparency carrier density, the gain compression factor, background absorption, the modal cross-section for free-carrier absorption, and the local photon density, respectively. All effective model parameters have been obtained by multiplying the material parameters with the vertical confinement factor $\Gamma = 0.0068$ calculated from the fundamental mode $\phi(y)$ of the vertical wave guide created by the epitaxial layer structure. Since our aim is the investigation of non-thermal effects, the temperature dependence of all parameters, in particular the temperature dependent contribution to the effective index (thermal lensing), is omitted in equation (2).

The traveling wave equations (1) are coupled to ordinary differential equations for the complex slowly varying amplitudes of the polarization fields $p^\pm$ [9],

$$\mathcal{D}u^\pm = \frac{g_r}{2}(u^\pm - p^\pm), \quad \partial_t p^\pm = \gamma(u^\pm - p^\pm) + i\delta\omega p^\pm, \tag{3}$$

which approximate the dispersion of the gain with a Loretzian of amplitude $g_r$, half width at half maximum $\gamma$, and relative central frequency $\delta\omega$.

The equations (1) for the optical field have to be supplemented by equations for the charged carrier densities. Due to computer restrictions, until now simulation tools based on the traveling wave model do not solve the full time-dependent drift-diffusion equations, as stationary models sometimes do [4, 18], but only a lateral diffusion equation for the excess carriers in the active layer [9, 19, 20]. Similarly, in our approach the vertically-averaged excess carrier density $N$ in the quantum well is determined from the effective nonlinear diffusion equation,

$$\partial_t N = \partial_x(D_{\text{eff}}(N)\partial_x N) + \frac{j(N)}{ed} - R(N) - R_{\text{stim}}, \tag{4}$$

where $D_{\text{eff}}(N) = (p_0 + N)\mu_p\partial_N\varphi_F(N)$ is a carrier dependent effective diffusion coefficient determined by the equilibrium hole carrier density $p_0$, the hole mobility in the active region $\mu_p$, and the Fermi voltage in the active layer $\varphi_F(N)$; $j(N)$ is the injection current density, whereas $R(N)$ and $R_{\text{stim}} = v_g\text{Re}\sum_{\nu=\pm} u^{\nu*}[gu^\nu - g_r(u^\nu - p^\nu)]$ are the non-radiative and spontaneous radiative, and the stimulated recombination rate, respectively [16]. As the carrier density gradient in the longitudinal direction is much smaller than the gradient in the lateral direction, the derivative $\partial_z N$ is neglected.

Time-dependent [9, 19, 20] and even stationary [21, 13] simulation tools commonly use a spatially constant injection current density below and a vanishing current density outside of the contact stripe as source term in equation (4). Such a constant-injection-current-density model oversimplifies the current flow and carrier transport in the device, because current spreading and current self-distribution are not taken into account [22], which are crucial for non-thermal blooming.

An improved model can be gained from the drift-diffusion equations if local charge neutrality is assumed, recombination in the bulk layer neglected and the conductivity in the n-doped region assumed to be infinitely high [16]. The injection current density entering equation (1) is accordingly given by the derivative of the quasi-Fermi potential $\varphi_p$ of the holes,

$$j = \sigma\partial_y\varphi_p|_{y=y_a} \tag{5}$$

at the upper boundary $y_a$ of the active layer adjacent to the p-doped region. The quasi-Fermi potential of the holes assumed to be continuous across hetero boundaries is obtained by solving a Laplace equation in the p-doped region,

$$\nabla(\sigma\nabla\varphi_p) = 0, \tag{6}$$

with the hole conductivity $\sigma$ and the boundary conditions

$$\varphi_p|_{y=y_a} = \varphi_F(N), \tag{7}$$

$\varphi_p = U_0$ at the p-contact, with $U_0$ beeing the bias voltage, and homogeneous Neumann conditions elsewhere. The carrier dependence of the injection current density is mediated by the boundary conditions (5) and (7). In such a way current spreading and current self-distribution are naturally taken into account.

# 3 Numerical simulation

Equations (1), (3), (4), and (6) are numerically solved by the software tool BALaser [14]. Details of the numerical methods employed can be found in [23, 15]. Here we present results of numerical experiments, where the value of the applied voltage $U_0$ was stepwise increased. For each bias step the simulation time was $8$ ns. Due to the fact that no assumption on stationarity was made as in

a previous study [4] the optical fields and power show strong dynamics. The time step used in the simulation was $\delta t = 16.7$ fs. Mean values for intensity and power were obtained by averaging the simulation results of every bias step over the last $5$ ns.

Firstly we will focus on a structure without implantation ($d_{\text{res}} = 1345$ nm) and apply a voltage of $U = 1.89$ V resulting in an injection current of $I = 24.1$ A and an average power of $P = 25.6$ W.
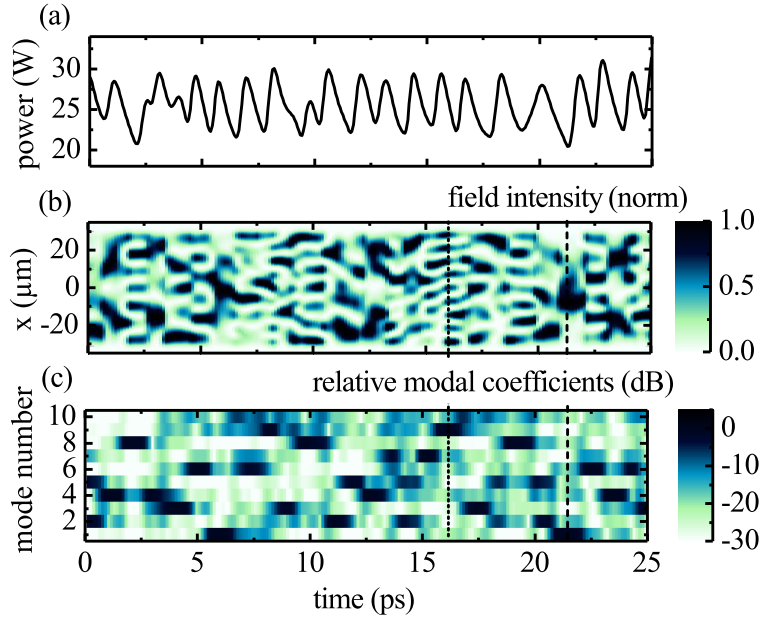


Figure 2: (a) Temporal evolution of the optical output power, (b) pseudo-color mapping of the near-field intensity distribution (normalized to maximum in every time step) and (c) similar mapping of the relative modal coefficients for $U = 1.89$ V ($I = 24.1$ A), $r_s = 5 \cdot 10^{-9}$ $\Omega$m$^2$, and $d_{\text{res}} = 1345$ nm. The vertical lines indicate stages where either a high order mode or the fundamental mode dominates.

The simulated time traces of output power and intensity profiles at the front facet are shown in Figs. 2(a) and 2(b), where a highly dynamic behavior is visible. Furthermore in 2(b) lateral structures with different numbers of intensity peaks can be identified that merge into each other over time. Furthermore the obtained spectrally resolved near-field intensity profiles from this simulation (Fig. 4(a)) show lateral structures with different numbers of intensity peaks at different wavelength as well. These observations suggest that the intensity peaks can be interpreted as different lateral modes and that the root-cause for the strong dynamics of output power and intensity profiles is indeed the interplay of multiple lateral waveguide modes. In order to explore this presumption, we perform a mode analysis introduced in Section 4.

## 4  Mode analysis

In order to reveal the root-cause for the strong power and intensity fluctuations visible in Figs. 2(a) and 2(b), the complex-valued field profile at the front facet, $z = L$, and a given instantaneous time $t$ is expanded in terms of the modes $\phi_m(x)$ of the Helmholtz equation for a hypothetical steady state,

$$\left[ k_0^{-2} \partial^2 / \partial x^2 + \langle n_{\text{eff}}(x) \rangle_t^2 \right] \phi_m(x) = \hat{n}_m^2 \phi_m(x), \tag{8}$$

where $x$ is the lateral coordinate, $\hat{n}_m$ is the modal index being the complex-valued eigenvalue and $\langle n_{\text{eff}}(x) \rangle_t^2 := [\bar{n} + \langle \Delta n_{\text{eff}}(x) \rangle_t]^2$ the time averaged effective index, which includes the same built-in modifications of the effective index, carrier induced index contributions as well as gain and losses as the traveling wave model and is calculated from the time averaged profiles of carrier density $\langle N \rangle_t$ and field intensity $\langle \|u\|^2 \rangle_t$ according to equation. (2).
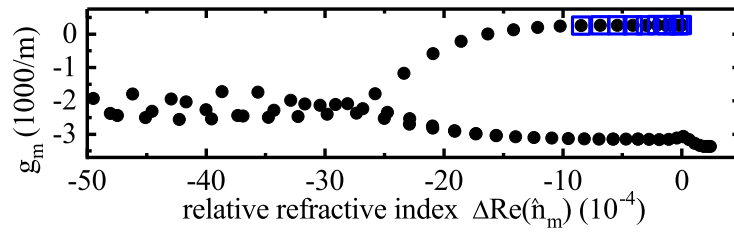
Figure 3: Real (abscissa) and imaginary (ordinate) eigenvalues of the modes obtained from the solution of the Helmholtz equation for $U = 1.89$ V ($I = 24.1$ A), $r_s = 5 \cdot 10^{-9}$ $\Omega m^2$, and $d_{res} = 1345$ nm. Eigenvalues of modes with a significant contribution to the field (cf. Fig. 7(c)) are marked blue.

For every time instance the complex optical field amplitude $u_{out}(x, t)$ emitted at the front facet can be expressed as a linear combination of the eigenfunctions $\phi_m$ of (8), $u_{out}(x, t) = \sum_m a_m(t)\phi_m(x, t)$ with the modal coefficients $a_m = \int \phi_m u_{out} \, dx / \int \phi_m \phi_m \, dx$.

In Fig. 2(c) the magnitudes of the relative modal coefficients $|a_m|^2 / \sum_m |a_m|^2$ are displayed versus time as a pseudo-color mapping. Only the $10$ modes with the highest gain have a significant contribution to the field (marked blue in Fig. 3). We see that the strong dynamic behavior of the emitted power and near-field intensity (see Fig. 2(a) and 2(b)) is a result of the alternate lasing of different lateral modes. At some time instances it can directly be traced back to the dynamic lateral structure of the intensity. For example, at $t = 16.2$ ps (dotted vertical line), the near-field in panel (b) has $9$ maxima and accordingly the $9^{th}$ mode has the highest contribution to the field, whereas at $t = 21.4$ ps (dashed vertical line) the near-field has one maximum and accordingly the fundamental mode has the highest contribution.
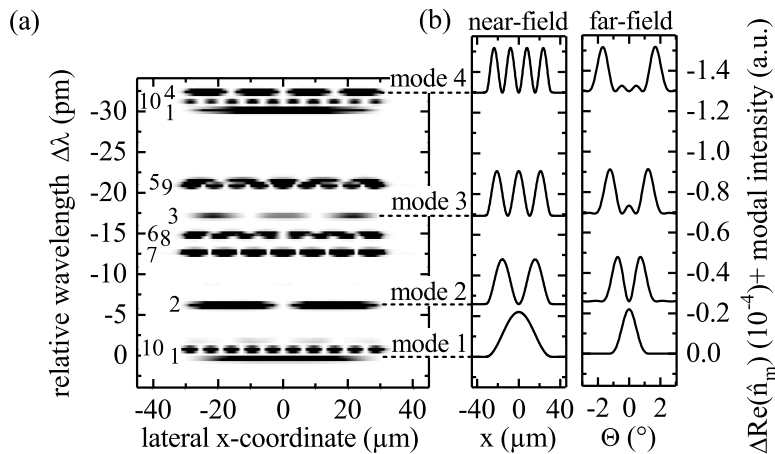


Figure 4: (a) Intensity distribution of the spectrally resolved complex near-field obtained by the traveling wave model as function of the wavelength relative to the peak wavelength of the fundamental mode. On the left side the lateral mode number is displayed. (b) near and far-field intensities of the first four lateral modes obtained by solving equation (8) vertically shifted according to their real part of the modal index relative to the real part of the index of the fundamental mode. $U = 1.89$ V ($I = 24.1$ A), $r_s = 5 \cdot 10^{-9}$ $\Omega m^2$, and $d_{res} = 1345$ nm.

The imaginary and real parts of the eigenvalues of (8) are displayed in Fig. 3 where the ordinate is the modal gain $g_m = 2k_0 \text{Im}(\hat{n}_m)$ and the abscissa the real part of the modal index relative to the

real part of the index of the fundamental mode, $\Delta \text{Re}(\hat{n}_m) = \text{Re}(\hat{n}_m) - \text{Re}(\hat{n}_1)$. In Fig. 4(a) the spectrally resolved near-field intensity profiles obtained from the traveling wave model by a Fourier transformation (FT) of $u_{\text{out}}(x, t)$ are shown. The lateral mode number is given on the left side. The longitudinal mode spacing of $\Delta\lambda_{\text{FT}}^{\text{long}} = 30$ pm is larger than the spacing of low order lateral modes and not all lateral modes displayed in Fig. 4(a) correspond to the same longitudinal mode.
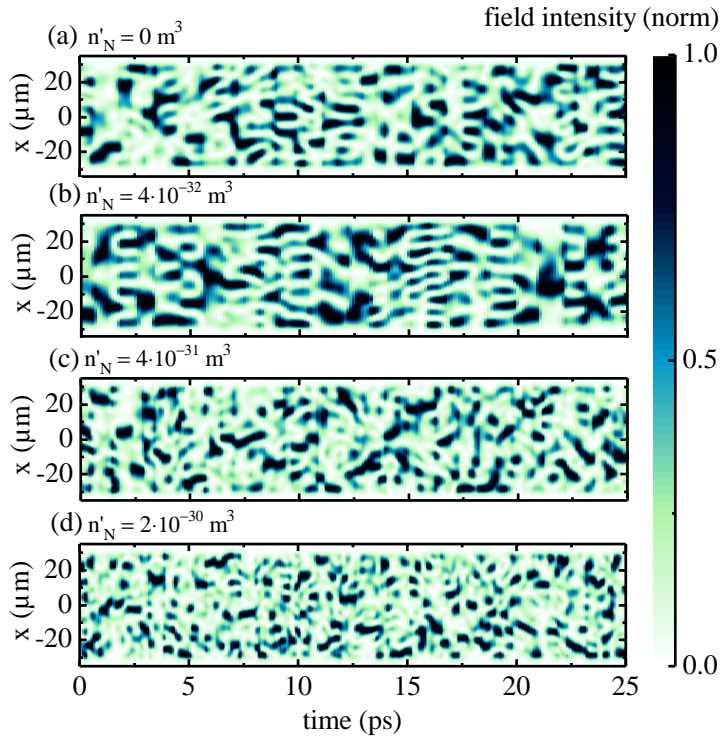


Figure 5: Pseudo-color mapping of the temporal near-field intensity evolution (normalized to maximum in every time step) for a differential index of (a) $n'_N = 0 \, \text{m}^3$, (b) $n'_N = 4 \cdot 10^{-32} \, \text{m}^3$ (replot from Fig. 2(b)), (c) $n'_N = 4 \cdot 10^{-31} \, \text{m}^3$ and (d) $n'_N = 2 \cdot 10^{-30} \, \text{m}^3$.

The lateral intensity profiles of the near and far-field of the first four modes with the highest gain according to Fig. 3 obtained from the solution of (8) are exemplary displayed in Fig. 4(b). The zero levels of the mode intensities are given by the relative real parts of the corresponding modal indices which can be converted into corresponding relative wavelengths $\Delta\lambda_m = \lambda_m - \lambda_1 = \lambda_0/n_g \cdot \text{Re}(\Delta\hat{n}_m)$ where $n_g = 3.92$ is the group index. As indicated by the dotted lines, these wavelength shifts agree very well with the FT peak wavelengths of the lateral modes for the same longitudinal mode. The same applies for the longitudinal mode spacing which matches the theoretical relation $\Delta\lambda_{\text{theory}}^{\text{long}} = \lambda_0^2/(2Ln_g)$. Thus, although no pre-assumptions were made regarding the optical field our result indicates that in lasers with a lateral waveguide a clear mode structure is visible which is neither destroyed by the dynamics nor by longitudinal effects.

Now we turn to the question of the role of the Kerr effect in this context. As stated in the introduction a Kerr-type nonlinearity is induced indirectly from the dependence of the refractive index on the carrier density. This effect is contained in our model and governed by the differential index $n'_N$. As the corresponding effective Kerr coefficient calculated according to [24] is several orders of magnitude larger than the absolute value of the material Kerr coefficient [25] the latter one can be ignored. The influence of the strength of the indirect Kerr effect is examined by varying $n'_N$ in Fig. 5. In the top panel (a) the Kerr effect is completely turned off ($n'_N = 0$). Here, the space-time structure of the field intensity is fully determined by the waveguide modes. This structure differs only marginally from our standard case of $n'_N = 4 \cdot 10^{-32} \, \text{m}^3$ (panel (b)) and we conclude that mode formation is still the dominating effect. However, with further increasing $n'_N$ the spatial and temporal scales of the intensity structures become smaller, panel (c) and (d). But it has to be pointed out, that the time scales are

so short that the indirect connection between intensity and carrier induced refractive index change is not instantaneous anymore as in the standard Kerr nonlinearity. Therefore, one can expect a different scenario, but a detailed analysis of this effect is beyond the scope of this paper.

We also investigated the sensitivity of the results to the choice of other parameters. An increased mobility of the holes in the active region that enters the effective diffusion coefficient in equation (4) is beneficial for suppressing higher order lateral modes, because fluctuations in the carrier density can be faster compensated for. However, only for a variation of the hole mobility of several orders of magnitude a significant influence could be found. Other parameters such as the gain compression factor $\epsilon_s$ or the free-carrier absorption coefficient $f_N$ have no significant impact on the lateral mode forming dynamics if varied within reasonable limits. The influence of further important parameters on the output field will be separately discussed in Section 5.

# 5  Far–field blooming

In what follows we investigate the impact of the injection current, an additional implantation beside the contact stripe and the series resistance below the contact stripe on the optical output field.
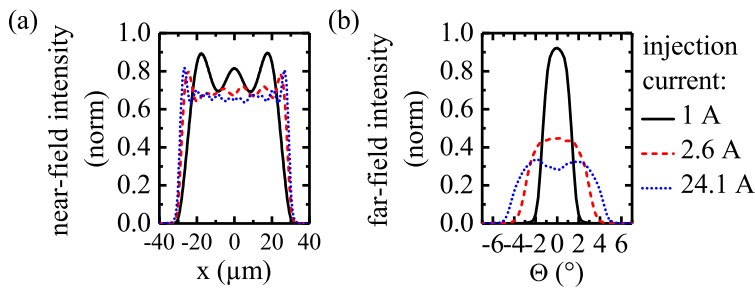


Figure 6: (a) Time averaged lateral near-field intensity and (b) far-field intensity distributions at the front facet for the total injection currents $I = 1$, 2.6, and 24.1 A. $r_s = 5 \cdot 10^{-9}\,\Omega\mathrm{m}^2$ and $d_{\mathrm{res}} = 1345\,\mathrm{nm}$.

In Fig. 6 the time averaged near- and far-field intensity distributions at the front facet are exemplarily displayed for the total injection currents $I = 1\,\mathrm{A}$, $2.6\,\mathrm{A}$ and $24.1\,\mathrm{A}$. From the time averaged near and far-field intensities at the front facet the full near-field width $w$ and far-field angle $\Theta$ containing $95\%$ of the power are calculated. The lateral beam quality can be specified from these parameters as the lateral beam parameter product BPP $= w\Theta/4$.



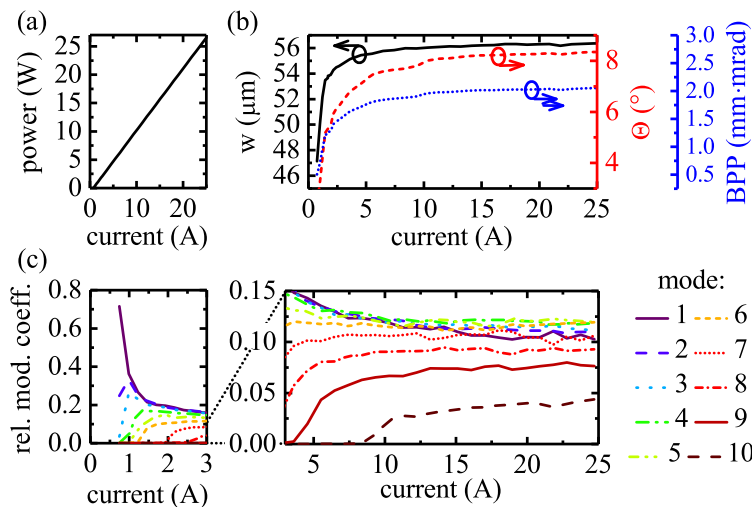Figure 7: (a) Power-current (PI) characteristics. (b) Lateral near-field width $w$ (black line – left axis), far-field angle $\Theta$ (red dashed – right axis) and beam parameter product BPP (blue dotted – rightmost axis) versus injection current. (c) Time averaged mean square values of the relative modal coefficients as function of the injection current. $r_s = 5 \cdot 10^{-9}\,\Omega\mathrm{m}^2$ and $d_{\mathrm{res}} = 1345\,\mathrm{nm}$.

Fig. 7(a) shows the dependence of the output power on the injection current and Fig. 7(b) the corresponding variation of the beam parameters. Both near-field width and far-field angle rise with increasing injection current, resulting in a degradation of the beam quality. Note that the relative rise of the far-field angle from threshold to high power amounts to $\approx 50\%$.
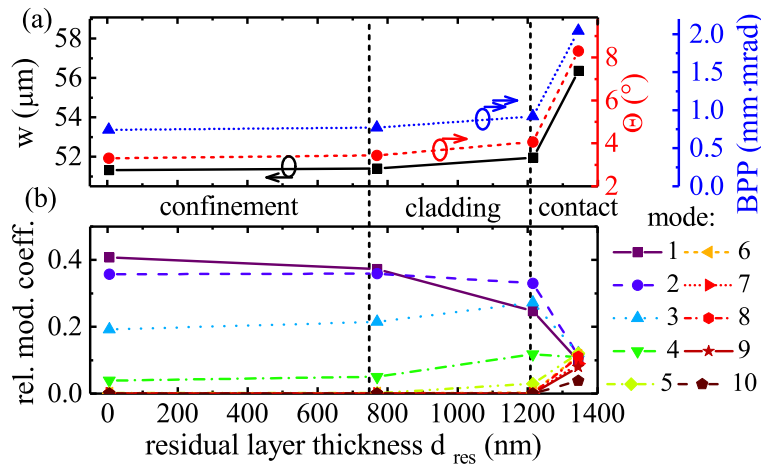


Figure 8: (a) Lateral near-field width $w$ (black line – left axis), far-field angle $\Theta$ (red dashed – right axis) and corresponding beam parameter product BPP (blue dotted – rightmost axis) and (b) relative modal coefficients as function of the residual layer thickness $d_{res}$ for $U = 1.89$ V. Series resistivity $r_s = 5 \cdot 10^{-9}$ $\Omega m^2$.

Directly above threshold ($I_{th} = 0.7$ A cf. Fig. 7(a)) laser emission is made up mostly by the first mode (Fig. 7(c)). With increasing current its relative contribution is diminished (without turning off completely), as more and more modes reach threshold. This behavior differs from what was published earlier [4] where at threshold the first 3 modes have an equal contribution to lasing and then consecutively turn off as more modes emerge. The rapid increase of contributing modes is taking place within the first 5 A where the first 9 modes are excited, so that the far-field angle is significantly broadened during this current span. A further abrupt rise of the far-field angle between 9.5 A and 10 A (Fig. 7(b)) can be traced back to the excitation of the 10th mode (Fig. 7(c)).
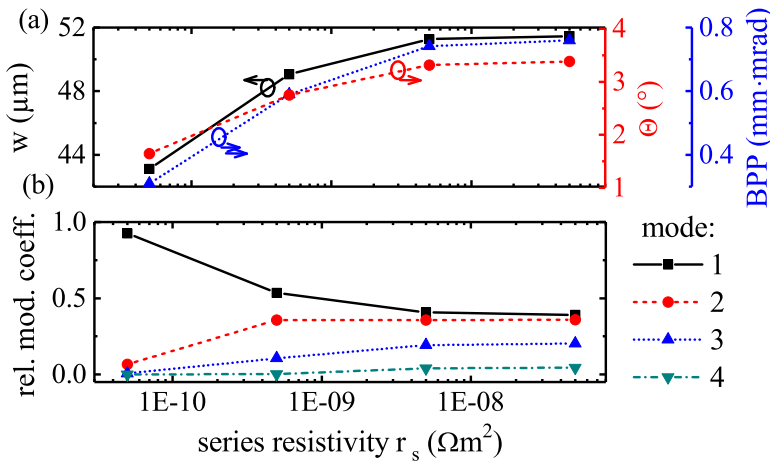


Figure 9: Lateral near-field width $w$ (black line – left axis), far-field angle $\Theta$ (red dashed – right axis) and beam parameter product BPP (blue dotted – rightmost axis) and (b) relative modal coefficients as function of the series resistivity $r_s$ for an injection current of $I = 20.0$ A corresponding to an output power of $P \approx 21.3$ W. Residual layer thickness $d_{res} = 5$ nm.

As a consequence of the previous findings, the suppression of higher order lateral modes is expected to improve the beam quality of the laser which will now be investigated in the following. A possibility to achieve this is an additional implantation beside the contact stripe [5]. As shown in Fig. 8(a), already an implantation of the contact layer, see also Fig. 1(c), drastically improves the beam quality, as the number of lateral lasing modes is decreased from 10 to 4 (Fig. 8(b)). In the absence of thermal lensing a further implantation of cladding and confinement layers leads only to minor improvements rendering deep implantation unnecessary for pulsed operation (if trenches close to the stripe are present). Note that the residual layer thicknesses of 5, 770, 1215 and 1345 nm result in currents of $I = 20.0$,

20.4, 21.5 and 24.1 A and powers of $P = 21.3$, 21.6, 22.8 and 25.6 W, respectively, for a constant $U = 1.89$ V.
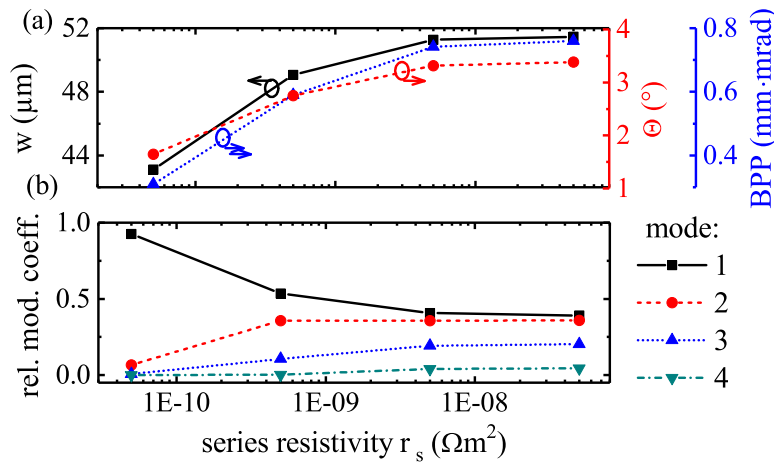


Figure 10: Lateral near-field width $w$ (black line – left axis), far-field angle $\Theta$ (red dashed – right axis) and beam parameter product BPP (blue dotted – rightmost axis) and (b) relative modal coefficients as function of the series resistivity $r_s$ for an injection current of $I = 20.0$ A corresponding to an output power of $P \approx 21.3$ W. Residual layer thickness $d_{res} = 5$ nm.

Due to the fact that the excitation of higher order modes is caused by the saturation of the gain in those parts of the active layer where the lower order mode intensity is high and a rise of the gain in the other parts, a suppression of spatial holeburning should result in an improved beam quality. In our previous study [26] we have demonstrated that a reduction of the p-layer resistivity $r_s$ results not only in an equalized carrier density below the contact stripe due to current self-distribution [27, 22] but can also lead to an improvement of the beam quality. Fig. 10(a) reveals that the near-field width $w$ and far-field angle $\Theta$ are decreased by reducing $r_s$. A modal analysis confirms that 4 lateral modes are lasing at $r_s = 5 \cdot 10^{-9}$ $\Omega m^2$ and the fundamental mode has a contribution of less than 50 % (Fig. 10(b)). However, at $r_s = 5 \cdot 10^{-11}$ $\Omega m^2$ 90 % of laser emission is made up by the first and 10 % by the second mode, so that the theoretical limit of the beam parameter product is nearly reached.

# 6 Conclusion

To summarize, BA lasers have been numerically simulated using an improved version of the software tool BALaser that properly describes the current flow in the p-doped layers as well as lateral and longitudinal spatial hole burning based on a traveling-wave model. We show that non-thermal far-field blooming can be understood on the basis of superposition of stationary modes despite the highly non-stationary behavior of broad-area lasers. To improve the beam quality, higher order lateral modes can be substantially suppressed by implanting the contact layer next to the injection stripe or by lowering the p-layer resistivity.

# Acknowledgment

# References

[1] P. Crump, S. Böldicke, C. M. Schultz, H. Ekhteraei, H. Wenzel, and G. Erbert, "Experimental and theoretical analysis of the dominant lateral waveguiding mechanism in 975 nm high power broad area diode lasers," *Semicond. Sci. Technol.* **27**, p. 045001, 2012.

[2] J. Piprek, "Self-consistent far-field blooming analysis for high-power Fabry-Pérot laser diodes," *Proc. SPIE* **8619**, p. 861910, 2013.

[3] S. Rauch, H. Wenzel, M. Radziunas, M. Haas, G. Tränkle, and H. Zimer, "Impact of longitudinal refractive index change on the near-field width of high-power broad-area diode lasers," *Appl. Phys. Lett.* **110**(26), p. 263504, 2017.

[4] J. Piprek and Z. M. S. Li, "On the importance of non-thermal far-field blooming in broad-area high-power laser diodes," *Appl. Phys. Lett.* **102**, p. 221110, 2013.

[5] M. Winterfeldt, P. Crump, S. Knigge, A. Maaßdorf, U. Zeimer, and G. Erbert, "High beam quality in broad area lasers via suppression of lateral carrier accumulation," *IEEE Photon. Techn. Lett.* **27**(17), pp. 1809–1812, 2015.

[6] V. I. Bespalov and V. I. Talanov, "Filamentary structure of light beams in nonlinear liquids," *JETP Lett.* **3**(11), pp. 307–310, 1966.

[7] G. H. B. Thompson, "A theory for filamentation in semiconductor lasers including the dependence of dielectric constant on injected carrier density," *Opt. Quant. Electron.* **4**(3), pp. 257–310, 1972.

[8] O. Hess, "Spatio-temporal complexity in multi-stripe and broad-area semiconductor lasers," *Chaos Solitons Fractals* **4**(8/9), pp. 1597–1618, 1994.

[9] C. Z. Ning, R. A. Indik, and J. V. Moloney, "Effective bloch equations for semiconductor lasers and amplifiers," *IEEE J. Quantum Electron.* **33**(9), pp. 1543–1550, 1997.

[10] H. Wenzel, P. Crump, H. Ekhteraei, C. Schultz, J. Pomplun, S. Burger, L. Zschiedrich, F. Schmidt, and G. Erbert, "Theoretical and experimental analysis of the lateral modes of high-power broad-area lasers," *Proc. NUSOD* **11**, pp. 10–11, 2011.

[11] H. Wenzel, "Basic aspects of high-power semiconductor laser simulation," *IEEE J. Sel. Top. Quantum Electron.* **19**(5), p. 1502913, 2013.

[12] J. R. Marciante and G. P. Agrawal, "Nonlinear mechanisms of filamentation in broad-area semiconductor lasers," *IEEE J. Quantum Electron.* **32**(4), pp. 590–596, 1996.

[13] C. Holly, S. Hengesbach, M. Traub, and D. Hoffmann, "Simulation of spectral stabilization of high-power broad-area edge emitting semiconductor lasers," *Optics Express* **21**(13), pp. 15553–15567, 2013.

[14] BALaser, "A software tool for simulation of dynamics in broad area semiconductor lasers. http://www.wias-berlin.de/software/balaser/."

[15] M. Radziunas, A. Zeghuzi, J. Fuhrmann, T. Koprucki, H.-J. Wünsche, H. Wenzel, and U. Bandelow, "Efficient coupling of inhomogeneous current spreading and electro-optical models for simulation of dynamics in broad-area semiconductor lasers," *Opt. and Quantum Electron.* **49**, p. 332, 2017.

[16] A. Zeghuzi, H. Wenzel, H.-J. Wünsche, M. Radziunas, U. Bandelow, and A. Knigge, "Modeling of current spreading in high-power broad-area lasers and its impact on the lateral far field divergence," *Proc. SPIE* **10526**, p. 105261H, 2018.

[17] P. Crump, G. Erbert, H. Wenzel, C. Frevert, C. M. Schultz, K.-H. Hasler, R. Staske, B. Sumpf, A. Maassdorf, F. Bugge, S. Knigge, and G. Tränkle, "Efficient high-power laser diodes," *IEEE J. Sel. Top. Quantum Electron.* **19**(4), p. 1501211, 2013.

[18] L. Borruel, S. Sujecki, P. Moreno, J. Wykes, M. Krakowski, B. Sumpf, P. Sewell, S.-C. Auzanneau, H. Wenzel, D. Rodríguez, T. M. Benson, E. C. Larkins, and I. Esquivias, "Quasi-3-D simulation of high-brightness tapered lasers," *IEEE J. Quantum Electron.* **40**(5), pp. 463–472, 2004.

[19] M. Lichtner, M. Radziunas, U. Bandelow, M. Spreemann, and H. Wenzel, "Dynamic simulation of high brightness semiconductor lasers," *Proc. NUSOD* , pp. 65–66, 2008.

[20] A. Pérez-Serrano, J. Javaloyes, and S. Balle, "Spectral delay algebraic equation approach to broad area laser diodes," *IEEE J. Sel. Topics Quantum Electron.* **19**(5), p. 1502808, 2013.

[21] H.-C. Eckstein and U. D. Zeitner, "Modeling electro-optical characteristics of broad area semiconductor lasers based on a quasi-stationary multimode analysis," *Optics Express* **21**(20), pp. 23231–23240, 2013.

[22] P. Eliseev, A. Glebov, and M. Osinski, "Current self-distribution effect in diode lasers: analytic criterion and numerical study," *IEEE J. Sel. Top. Quantum Electron.* **3**(2), pp. 499–506, 1997.

[23] M. Radziunas and R. Ciegis, "Effective numerical algorithm for simulations of beam stabilization in broad area semiconductor lasers and amplifiers," *Math. Mod. and Anal.* **19**(5), pp. 627–646, 2014.

[24] H. Wenzel and A. Zeghuzi, "High power lasers," in *Handbook of Optoelectronic Device Modeling and Simulation: Lasers, Modulators, Photodetectors, Solar Cells, and Numerical Methods-Volume Two*, J. Piprek, ed., ch. 27, CRC Press, 2017.

[25] M. Sheik-Bahae, D. C. Hutchings, D. J. Hagan, and E. W. Van Stryland, "Dispersion of bound electronic nonlinear refraction in solids," *IEEE J. Quantum Electron.* **27**(6), pp. 1296–1309, 1991.

[26] A. Zeghuzi, M. Radziunas, H. J. Wünsche, A. Klehr, H. Wenzel, and A. Knigge, "Influence of nonlinear effects on the characteristics of pulsed high-power BA DBR lasers," *Opt. and Quantum Electron.* **50**, p. 88, 2018.

[27] W. B. Joyce, "Role of the conductivity of the confining layers in DH-laser spatial hole burning effects," *IEEE J. Quantum Electron.* **18**(12), pp. 2005–2009, 1982.